

# Contrast between Surface Plasmon Polariton-Mediated Extraordinary Optical Transmission Behavior in Epitaxial and Polycrystalline Ag Films in the Mid- and Far-Infrared Regimes

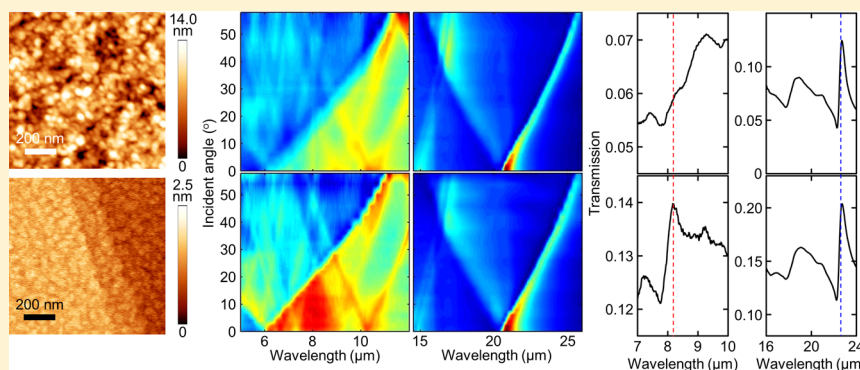
Bo-Hong Li,<sup>†,||</sup> Charlotte E. Sanders,<sup>‡,||</sup> James McIlhargey,<sup>‡</sup> Fei Cheng,<sup>†</sup> Changzhi Gu,<sup>†</sup> Guanhua Zhang,<sup>†,‡</sup> Kehui Wu,<sup>†</sup> Jisun Kim,<sup>‡</sup> S. Hossein Mousavi,<sup>‡</sup> Alexander B. Khanikaev,<sup>‡</sup> Yu-Jung Lu,<sup>§</sup> Shangjr Gwo,<sup>§</sup> Gennady Shvets,<sup>\*,‡</sup> Chih-Kang Shih,<sup>\*,‡</sup> and Xianggang Qiu<sup>\*,†</sup>

<sup>†</sup>Beijing National Laboratory for Condensed Matter Physics and Institute of Physics, Chinese Academy of Sciences, Beijing 100190, China

<sup>‡</sup>Department of Physics, The University of Texas at Austin, Austin, Texas 78712, United States

<sup>§</sup>Department of Physics, National Tsing-Hua University, Hsinchu 30013, Taiwan

**S** Supporting Information



**ABSTRACT:** In this Letter we report a comparative study, in the infrared regime, of surface plasmon polariton (SPP) propagation in epitaxially grown Ag films and in polycrystalline Ag films, all grown on Si substrates. Plasmonic resonance features are analyzed using extraordinary optical transmission (EOT) measurements, and SPP band structures for the two dielectric/metal interfaces are investigated for both types of film. At the Si/Ag interface, EOT spectra show almost identical features for epitaxial and polycrystalline Ag films and are characterized by sharp Fano resonances. On the contrary, at the air/Ag interface, dramatic differences are observed: while the epitaxial film continues to exhibit sharp Fano resonances, the polycrystalline film shows only broad spectral features and much lower transmission intensities. In corroboration with theoretical simulations, we find that surface roughness plays a critical role in SPP propagation for this wavelength range.

**KEYWORDS:** Surface plasmon polaritons, enhanced optical transmission, surface roughness, epitaxial Ag film

Surface plasmon polaritons (SPPs) are hybrid photon-electron oscillations propagating along the interface between a metallic ( $\epsilon < 0$ ) and a dielectric ( $\epsilon > 0$ ) material. Because of the finite penetration of light into metal, SPPs are confined at a length scale much smaller than the wavelength of incident light, and this tight confinement is expected to enable the integration of diffraction-limited optical structures and much smaller electronic components.<sup>1–5</sup> Many novel devices using the exotic properties of SPPs have been proposed or demonstrated.<sup>3,6–15</sup> However, most plasmonic devices to date have been based on granular polycrystalline metal films, in which scattering losses at grain boundaries<sup>16</sup> and rough surfaces can be considerable. These losses limit their technological potential. Intense research has been made to improve the surface smoothness of metal films. For example, the template stripping method<sup>17</sup> has been utilized to produce smooth

patterned surfaces on one side of a metal film, and more recently, Au platelets with atomic smoothness on two surfaces have been created.<sup>18</sup> However, a better plasmonic platform is epitaxially grown, atomically smooth metallic film on a dielectric substrate. The superiority of this type of film has recently been dramatically demonstrated, with the continuous-wave operation of a plasmonics-based nanolaser in the visible regime. The laser consisted of atomically flat epitaxial Ag film on Si as a plasmonic platform and InGaN as a gain medium.<sup>19</sup> What makes the nanolaser achievement particularly striking is the fact that, in the visible spectral region ( $\sim 500$  nm) at which

**Received:** August 14, 2012

**Revised:** November 3, 2012

**Published:** November 6, 2012

the nanolaser was demonstrated, the granular structure of a polycrystalline film results in significant scattering loss and inhibits lasing. Since there are also many important applications for plasmonics in the mid- and far-infrared regimes,<sup>20–26</sup> it is important to determine whether such a dramatic difference persists between losses in epitaxial and polycrystalline films at these longer wavelength ranges.

In this Letter we report on the use of angle-resolved spectroscopy of SPP-mediated extraordinary optical transmission (EOT)<sup>27–29</sup> to investigate the plasmonic properties of epitaxial and polycrystalline Ag films. So as to permit comparison between them we prepared epitaxial and polycrystalline films with the same thickness and patterned them with identical hole arrays using the same fabrication process. The SPP modes at the air/Ag interface exhibited dramatic differences in each of the two films in the mid-infrared (MIR) regime. However, these differences vanished for the SPP modes at the Si/Ag interface in the far-infrared (FIR) regime. We attribute these contrasting behaviors in the MIR and FIR regimes to the different amounts of surface roughness at the two interfaces of each of the two kinds of films. Simulated spectra computed by the finite element method (FEM), taking a perfect electric conductor (PEC) as an approximation of the Ag film, agree well with the observed spectra of epitaxial Ag films. To simulate spectra for films with surface roughness, we inserted into our simulation a lossy layer between the air and the PEC film. By increasing the loss factor of this layer, we simulated a gradual transition from the spectrum of an epitaxial-like film to that of a polycrystalline-like film.

To grow epitaxial Ag film on Si substrates we follow the two-step growth process which has been described in the literature: low-temperature deposition followed by annealing at higher temperature.<sup>19,30</sup> By contrast with the film used in the recent work on nanolasing,<sup>19</sup> however, the thickness in this case is 80 nm—thicker by a factor of 3. Moreover, there is no Ge capping layer atop. At the thickness of 80 nm, even without the Ge capping layer, the film is stable enough against dewetting (due to a relatively larger kinetic barrier) to allow for fabrication and measurements within two weeks after the initial growth. However, as we discuss below, prolonged exposure to atmosphere does eventually cause the film to roughen. Polycrystalline films—also 80 nm thick—are grown by thermal evaporation onto a Si wafer with native oxide on the surface. Both the polycrystalline and epitaxial films are patterned with a square array of circular holes occupying an area of about  $5 \times 5 \text{ nm}^2$  using ultraviolet photolithography and reactive ion etching. The hole diameter  $d$  and the period  $a$  of the arrays are 3 and 6  $\mu\text{m}$ , respectively.

Figure 1a is an atomic force microscopy (AFM) image of the epitaxial film showing atomically smooth surface with low root-mean-square (RMS) surface roughness ( $\sim 0.37 \text{ nm}$ ). In Figure 1b an AFM image of polycrystalline Ag film shows granular features with much higher RMS surface roughness ( $\sim 2 \text{ nm}$ ).

Angle-resolved infrared transmission spectra in the wavelength range 4–28  $\mu\text{m}$  were obtained using a Fourier transform infrared spectrometer (FTIR). The measurements were taken immediately after the fabrication process, before significant degradation of the epitaxial Ag film in air could occur. Spectra from the epitaxial and polycrystalline films were acquired using identical measurement processes. The samples lay in the  $x$ - $y$  plane, rotating around the  $y$ -axis by  $2^\circ$  increments (Figure S1d in the Supporting Information). The incident beam was focused on the sample and was limited by a 5-mm-diameter

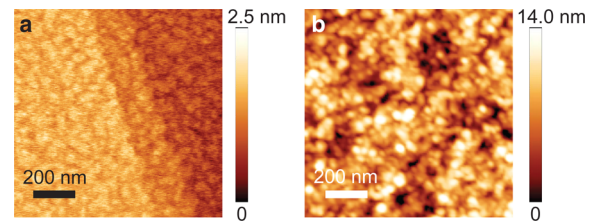


**Figure 1.** AFM images of Ag films. (a) AFM image of epitaxial Ag film showing RMS surface roughness  $\sim 0.37 \text{ nm}$ . Scale bar, 200 nm. (b) AFM image of polycrystalline Ag film showing RMS surface roughness  $\sim 2 \text{ nm}$ . Scale bar, 200 nm. (a,b) Scan area,  $1 \times 1 \mu\text{m}^2$ .

diaphragm. The relative transmission intensities of the Ag films were obtained by normalizing the transmission spectra of the samples with those of a bare Si substrate. The incoming beam impinging on the samples was in transverse-magnetic (TM) polarization: the direction of electric field  $E$  was in the incident ( $x$ - $z$ ) plane (Figure S1d in the Supporting Information).

Shown in Figure 2 are experimental and simulated transmission spectra summarized in four columns and three rows. The top and middle rows show the data acquired from perforated polycrystalline and epitaxial films, respectively, while the bottom row shows simulated transmission spectra for the same structures, calculated using COMSOL. The two left columns are in false color, containing angle-resolved spectra from  $0^\circ$  to  $60^\circ$  with a  $2^\circ$  step. Notice that the color scales for the polycrystalline and epitaxial Ag films are different: this is so that the respective band structures can be seen easily. (Selected raw data in stacked plots are shown in Figure S3 of the Supporting Information.) The two right columns are the individual spectra acquired at  $20^\circ$  (spectra at other angles are shown in Figure S4 of the Supporting Information).

For a square lattice, the reciprocal lattice vector is  $\vec{G}^{m,n} = m(2\pi/a)\hat{x} + n(2\pi/a)\hat{y}$ , where  $m$  and  $n$  are integers. An SPP can be excited when its momentum satisfies  $\vec{k}_{\text{SPP}}^{m,n} = \vec{k}_x + \vec{G}^{m,n}$ , where  $k_x \equiv |\vec{k}_x| \equiv k_0 \sin \theta$  is the component of the incident wave vector  $k_0 = 2\pi/\lambda$  projected onto the incident interface,  $\lambda$  is the wavelength measured *in vacuo*, and  $\theta$  is the incident angle (schematic in Figure S1d of the Supporting Information). The SPP bands can be indexed as Si( $m,n$ ) or air( $m,n$ ), for SPPs propagating at the Si/Ag or air/Ag interface, respectively. The SPP dispersion relation can be described by  $k_{\text{SPP}}^{m,n} \equiv |k_{\text{SPP}}^{m,n}| = k_0(\epsilon_m \epsilon_d / (\epsilon_m + \epsilon_d))^{1/2}$ , where  $\epsilon_m$  and  $\epsilon_d$  are the respective dielectric constants of the metal and dielectric. In the MIR and FIR regimes,  $\epsilon_d = 1$  for air and  $\epsilon_d = 11.9$  for Si, and  $-\text{Re}(\epsilon_m) \gg \epsilon_d$  for Ag; this means that  $\text{Re}(k_{\text{SPP}}^{m,n}) = k_0(\epsilon_d)^{1/2}$ , so Ag can be modeled as a PEC ( $\epsilon_{\text{PEC}} \rightarrow -\infty$ ) in these regimes. The analytically computable curves, with Ag treated as a PEC, are shown as solid lines in Figures 2c,f and can be identified as the sharp borders across which the transmission changes rapidly. An EOT peak is often accompanied by a transmission minimum, known as Wood's anomalies.<sup>31,32</sup> The sharpness of the transmission change across the SPP bands is determined by the propagation length of the SPPs, which is in turn determined by the radiative and ohmic losses of the leaky SPPs as well as by the scattering of SPPs at imperfections in patterned metal film. One important source of inelastic scattering is the surface roughness of the metal film, and it is instructive to compare the sharpness of the transmission features in the polycrystalline and epitaxial Ag films. The propagation length is proportional to the SPPs' lifetime  $\tau_{\text{SPP}}^{m,n}(k_x) \equiv 1/\text{Im}(\omega^{m,n})$ , which is computed from the complex angular frequency  $\omega_{\text{SPP}}^{m,n}(k_x) \equiv \text{Re}(\omega^{m,n}) +$

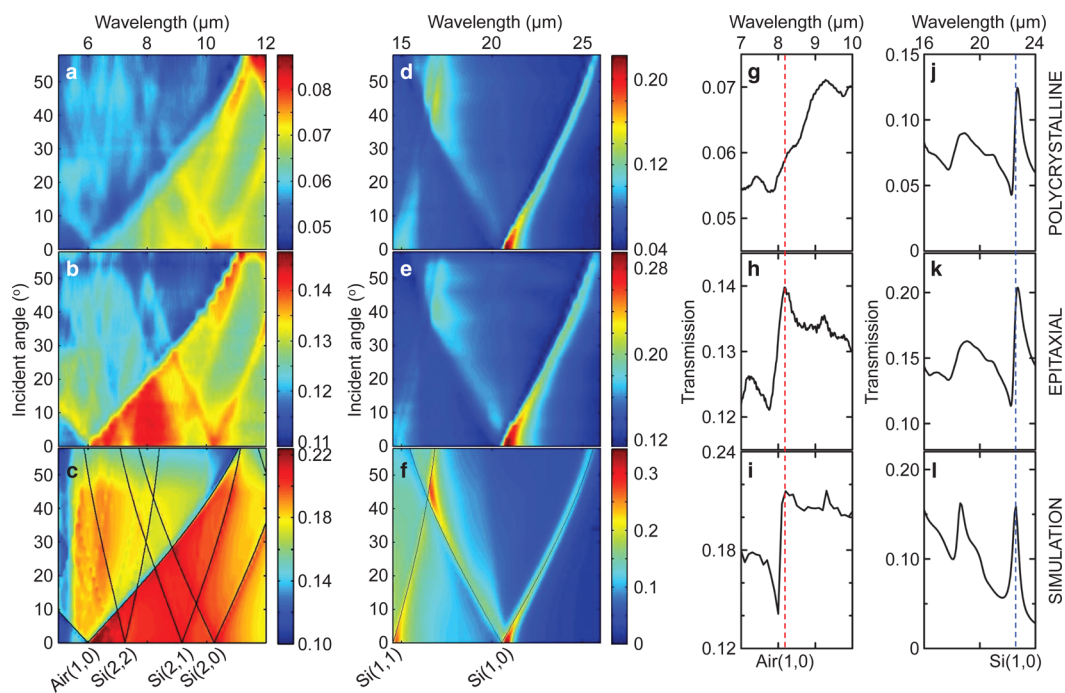


**Figure 2.** Experimental and simulated angle-resolved EOT transmission spectra in the infrared regime. (top and middle rows) Experimental angle-resolved infrared transmission spectra under TM-polarized illumination for perforated polycrystalline (top row) and epitaxial (middle row) Ag films. (bottom row) Simulation results from the commercial software package COMSOL, using the real geometric and material parameters except for the substitution of a PEC film for the Ag film. Both perforated Ag films (top and middle rows) and the PEC films (bottom row) have a thickness of 80 nm, a lattice period of 6  $\mu\text{m}$ , and a hole diameter of 3  $\mu\text{m}$ . (a–f) Contour plot with intensities indicated by false color. Theoretical SPP bands (black solid) are superposed on (c,f), with different SPP modes indexed by Si( $m,n$ ) or air( $m,n$ ). (g–l) Individual transmission spectra acquired at 20°. The dashed lines are to guide the eye for the air(1,0) (red) and Si(1,0) (blue) modes, respectively.

$i\text{Im}(\omega^{m,n})$  of the leaky SPPs by solving the eigenvalue Maxwell's equations<sup>33</sup> with radiative boundary conditions set at infinity.

Note that the Wood's anomalies bands must be distinguished from those of the leaky SPPs, although they can be very close to each other when the perforated holes are small compared with the resonant wavelength and when the metal's optical properties are close to those of a PEC. Because in those instances the SPP and Wood's anomalies bands run close and parallel to each other, a rapid change in intensity across the SPP bands is observed; this is the well-known Fano profile,<sup>32,34–36</sup> as shown in Figure 2. More remarkably, the SPP bands and Wood's anomalies bands can cross each other, resulting in an abrupt change in transmission along the SPP dispersion curves. This is observed in the vicinity of  $\lambda \approx 16.4 \mu\text{m}$  and  $\theta \approx 40^\circ$  (Figures 2d–f), the crossing point of Si(1,  $\pm 1$ ) and Si(-1,0) bands. Specifically, the Si(-1,0) band that starts out as relatively “dark” (low transmission) for small incident angles abruptly turns “bright” (high transmission) around  $\theta = 30^\circ$ . On the contrary, the Si(1,  $\pm 1$ ) band that starts out as relatively “bright” for small incident angles turns abruptly “dark” around  $\theta = 40^\circ$ . In Figure S3 of the Supporting Information, we show more detailed angle-resolved spectra in stacked plots to illustrate these behaviors.

In the FIR regime (14–26  $\mu\text{m}$  wavelength range) (Figures 2d–f; j–l), transmission intensity is about 30% higher for the epitaxial film, but the shapes of the transmission spectra from the polycrystalline and epitaxial Ag films exhibit little difference from each other. It is to be noted that in this regime EOT is mediated by SPPs propagating along the Si/Ag interface (e.g., Si(1,0) and Si(1,1) bands). The fairly good agreement between experimental and simulated FIR spectra, with regard to

wavelength and angle-dependence as well as transmission amplitude, suggests that the Si/Ag interface is rather smooth for both polycrystalline and epitaxial Ag films. As one moves to shorter wavelengths, from lower-order to higher-order Si( $m,n$ ) bands and eventually to the air(1,0) band, there is a systematic trend of degradation in the transmission signal of the polycrystalline film as compared with that of the epitaxial film (Figures 2a,b). The overall intensity for these bands is about a factor of 2 lower in the polycrystalline film. Moreover, plasmonic resonance features are much weaker in the polycrystalline film (note that the color scale for polycrystalline film is enhanced to show subtle features). The difference between the spectra from the epitaxial and polycrystalline films is particularly pronounced for the air(1,0) band (Figures 2g,h). Specifically, for epitaxial Ag film the transition from baseline to peak transmission occurs very rapidly as a function of wavelength (Figure 2h), in agreement with the simulation results shown in Figure 2i. For the polycrystalline film, the air(1,0) band appears as only a weak shoulder without any sharp resonances (Figure 2g). From the microscopic standpoint, it appears reasonable that the morphological difference between polycrystalline and epitaxial films should manifest itself in the quality of the air/Ag interface much more than the Si/Ag interface.

Much more detailed angle-dependent spectra are shown in Figure S4 of the Supporting Information. All of these spectra exhibit the same features as those just described, with the epitaxial film showing significantly sharper spectral features and higher overall transmission intensity for the air(1,0) band. In addition, we also measured the transmission spectra of the same epitaxial Ag film sample after prolonged exposure—nearly two

years—to air at room temperature. The degradation of the surface uniformity can be seen in the SEM image (Figure S1c in the Supporting Information). As discussed in the Supporting Information, the air(1,0) band after two years no longer exhibits a sharp resonant edge, but instead displays features similar to those of the polycrystalline Ag film. This result reaffirms the importance of surface smoothness to low-loss SPP propagation at the air/Ag interface.

To test the validity of our hypotheses, we have modeled the scattering of the air-side SPPs due to surface roughness by introducing into our simulation an artificial lossy layer of thickness  $t = 2 \mu\text{m}$  immediately adjacent to the PEC on the air side. The dielectric permittivity tensor of the lossy layer is chosen to be  $\epsilon_{xx} = \epsilon_{yy} = 1$ ,  $\epsilon_{zz} = 1 - i\gamma$ , where  $\gamma < 1$  is the loss factor of the layer. The physical justification for our choice of permittivity tensor is as follows. The electric field of the air-side SPPs propagating along the air/PEC interface is predominantly in the  $z$ -direction. Therefore, by introducing a small loss through the  $\epsilon_{zz}$  component of the tensor we effectively reduce the propagation length of the air-side SPPs without causing any damping or reflection of the incident wave, which—at least for small incident angles  $\theta$ —is primarily polarized along the  $x$ -direction. A simple but instructive expression can be derived for the wave vector of an SPP propagating at the interface between two semi-infinite media, a metal with the dielectric permittivity  $\epsilon_m$  and an anisotropic damping layer with the permittivity tensor just described:

$$k_{\text{SPP}} = k_0 \sqrt{\frac{\epsilon_m(\epsilon_z^3 - \epsilon_{xx}\epsilon_{zz}\epsilon_m)}{(\epsilon_{zz}^3 - \epsilon_{xx}\epsilon_m^2)}}$$

For very large values of  $|\epsilon_m| \gg 1$ , typical of the infrared regime, we find that the propagation length  $L_{\text{SPP}} = 1/\text{Im}(k_{\text{SPP}})$  is controlled by the  $\epsilon_{zz}$  component according to  $L_{\text{SPP}} \approx (\lambda_0/2\pi)/\text{Im}((\epsilon_{zz})^{1/2})$ . The simulated transmission curves (Figure 3a)

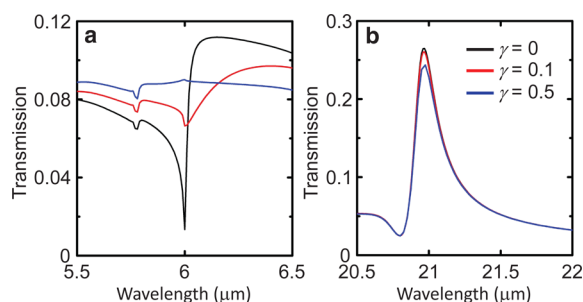


**Figure 3.** Simulated effects of a lossy layer at the air/PEC interface. Transmission is shown for an adhesion layer inserted between the air and PEC film with various loss factors. (a) air(1,0) mode. (b) Si(1,0) mode. The components of the permittivity tensor  $\epsilon_{xx} = \epsilon_{yy} = 1$  and  $\epsilon_{zz} = 1 - i\gamma$ . Loss factor  $\gamma = 0$  (black),  $\gamma = 0.1$  (red), and  $\gamma = 0.5$  (blue).

show clearly that the value of  $\gamma$  affects the normal transmission in the MIR regime by spectrally broadening the resonant peak from low to high transmission. At the same time, there is practically no effect of  $\gamma$  on FIR transmission (Figure 3b), because the latter is mediated by the Si-side SPPs, which are unaffected by the anisotropic damping layer.

In summary, by using angle-resolved EOT measurements in the infrared regime, we have shown the contrasting behavior of SPPs in epitaxial and polycrystalline Ag films on Si substrates. For atomically smooth epitaxial Ag film, we observe significant scattering reduction for air-side SPPs, which manifests as

spectrally sharp EOT features. On the contrary, polycrystalline Ag films show much weaker resonance at the air/Ag interface. At the Si/Ag interface, both the polycrystalline and the epitaxial films have smooth interfaces; consequently, EOT mediated by SPPs propagating at this interface exhibits high-quality sharp spectral features for both types of film. Furthermore, we have developed a model which accounts for the significant observed damping in polycrystalline films at the air/Ag interface. Our results demonstrate that surface roughness can be the crucial scattering loss mechanism in longer wavelength ranges.

## ■ ASSOCIATED CONTENT

### Supporting Information

SEM images of perforated Ag films and the experimental configuration, AFM images of the epitaxial and polycrystalline Ag films, angle-resolved experimental and simulated transmission spectra in stacked plots, and individual spectra at several different incident angles for the air(1,0) band. This material is available free of charge via the Internet at <http://pubs.acs.org>.

## ■ AUTHOR INFORMATION

### Corresponding Author

\*E-mail: [gena@physics.utexas.edu](mailto:gena@physics.utexas.edu); [shih@physics.utexas.edu](mailto:shih@physics.utexas.edu); [xgqiu@iphy.ac.cn](mailto:xgqiu@iphy.ac.cn).

### Author Contributions

||These authors contributed equally to this work.

### Notes

The authors declare no competing financial interest.

## ■ ACKNOWLEDGMENTS

We thank Peter Nordlander for useful discussions. Research activities at IOP-CAS are supported by Ministry of Science and Technology (973 Projects Nos. 2009CB929100 and 2012CB921302) and National Science Foundation of China (Grant Nos. 91121004 and 10974241), Chinese Academy of Sciences. Research activities at UT-Austin are supported by NSF Grants (NSF Grants Nos. DGE-0549417, DMR-0906025, and CMMI-0928664) and the Welch Foundation (Grant No. F-1672). Research activities at NTHU are supported in part by the National Science Council, Taiwan (Grant No. NSC-100-2120-M-007-001).

## ■ REFERENCES

- (1) Ozbay, E. *Science* **2006**, *311*, 189–193.
- (2) Brongersma, M. L.; Shalae, V. M. *Science* **2010**, *328*, 440–441.
- (3) Walters, R. J.; van Loon, R. V. A.; Brunets, I.; Schmitz, J.; Polman, A. *Nat. Mater.* **2010**, *9*, 21–25.
- (4) Schuller, J. A.; Barnard, E. S.; Cai, W.; Jun, Y. C.; White, J. S.; Brongersma, M. L. *Nat. Mater.* **2010**, *9*, 193–204.
- (5) Atwater, H. A.; Polman, A. *Nat. Mater.* **2010**, *9*, 205–213.
- (6) Economou, E. N. *Phys. Rev.* **1969**, *182*, 539–554.
- (7) Shvets, G. *Phys. Rev. B* **2003**, *67*, 035109.
- (8) Barnes, W. L.; Dereux, A.; Ebbesen, T. W. *Nature* **2003**, *424*, 824–830.
- (9) Melville, D.; Blaikie, R. *Opt. Express* **2005**, *13*, 2127–2134.
- (10) Fang, N.; Lee, H.; Sun, C.; Zhang, X. *Science* **2005**, *308*, 534–537.
- (11) Alù, A.; Engheta, N. *J. Opt. Soc. Am. B* **2006**, *23*, 571–583.
- (12) Shin, H.; Fan, S. *Phys. Rev. Lett.* **2006**, *96*, 073907.
- (13) Korobkin, D.; Urzhumov, Y.; Shvets, G. *J. Opt. Soc. Am. B* **2006**, *23*, 468–478.

- (14) Koller, D. M.; Hohenau, A.; Ditzlbacher, H.; Galler, N.; Reil, F.; Aussenegg, F. R.; Leitner, A.; List, E. J. W.; Krenn, J. R. *Nat. Photon.* **2008**, *2*, 684–687.
- (15) Garcia-Vidal, F. J.; Martin-Moreno, L.; Ebbesen, T. W.; Kuipers, L. *Rev. Mod. Phys.* **2010**, *82*, 729–787.
- (16) Kuttge, M.; Vesseur, E. J. R.; Verhoeven, J.; Lezec, H. J.; Atwater, H. A.; Polman, A. *Appl. Phys. Lett.* **2008**, *93*, 113110.
- (17) Nagpal, P.; Lindquist, N. C.; Oh, S.-H.; Norris, D. J. *Science* **2009**, *325*, 594–597.
- (18) Huang, J.-S.; Callegari, V.; Geisler, P.; Brüning, C.; Kern, J.; Prangma, J. C.; Wu, X.; Feichtner, T.; Ziegler, J.; Weinmann, P.; Kamp, M.; Forchel, A.; Biagioni, P.; Sennhauser, U.; Hecht, B. *Nat. Commun.* **2010**, *1*, 150.
- (19) Lu, Y.-J.; Kim, J.; Chen, H.-Y.; Wu, C.; Dabidian, N.; Sanders, C. E.; Wang, C.-Y.; Lu, M.-Y.; Li, B.-H.; Qiu, X.; Chang, W.-H.; Chen, L.-J.; Shvets, G.; Shih, C.-K.; Gwo, S. *Science* **2012**, *337*, 450–453.
- (20) Tetz, K. A.; Pang, L.; Fainman, Y. *Opt. Lett.* **2006**, *31*, 1528–1530.
- (21) Adato, R.; Yanik, A. A.; Amsden, J. J.; Kaplan, D. L.; Omenetto, F. G.; Hong, M. K.; Erramilli, S.; Altug, H. *Proc. Natl. Acad. Sci. U.S.A.* **2009**, *106*, 19227–19232.
- (22) Schnell, M.; Alonso-Gonzalez, P.; Arzubiaga, L.; Casanova, F.; Hueso, L. E.; Chuvilin, A.; Hillenbrand, R. *Nat. Photon.* **2011**, *5*, 283–287.
- (23) Lee, S. J.; Ku, Z.; Barve, A.; Montoya, J.; Jang, W.-Y.; Brueck, S. R. J.; Sundaram, M.; Reisinger, A.; Krishna, S.; Noh, S. K. *Nat. Commun.* **2011**, *2*, 286.
- (24) Jackson, S. D. *Nat. Photon.* **2012**, *6*, 423–431.
- (25) Yao, Y.; Hoffman, A. J.; Gmachl, C. F. *Nat. Photon.* **2012**, *6*, 432–439.
- (26) Schliesser, A.; Picque, N.; Hansch, T. W. *Nat. Photon.* **2012**, *6*, 440–449.
- (27) Ebbesen, T. W.; Lezec, H. J.; Ghaemi, H. F.; Thio, T.; Wolff, P. A. *Nature* **1998**, *391*, 667–669.
- (28) Ghaemi, H. F.; Thio, T.; Grupp, D. E.; Ebbesen, T. W.; Lezec, H. J. *Phys. Rev. B* **1998**, *58*, 6779–6782.
- (29) Gao, H.; Henzie, J.; Odom, T. W. *Nano Lett.* **2006**, *6*, 2104–2108.
- (30) Smith, A. R.; Chao, K.-J.; Niu, Q.; Shih, C.-K. *Science* **1996**, *273*, 226–228.
- (31) Sarrazin, M.; Vigneron, J.-P.; Vigoureux, J.-M. *Phys. Rev. B* **2003**, *67*, 085415.
- (32) Genet, C.; van Exter, M. P.; Woerdman, J. P. *Opt. Commun.* **2003**, *225*, 331–336.
- (33) Mousavi, S. H.; Khanikaev, A. B.; Neuner, B.; Avitzour, Y.; Korobkin, D.; Ferro, G.; Shvets, G. *Phys. Rev. Lett.* **2010**, *105*, 176803.
- (34) Fano, U. *Phys. Rev.* **1961**, *124*, 1866–1878.
- (35) Luk'yanchuk, B.; Zheludev, N. I.; Maier, S. A.; Halas, N. J.; Nordlander, P.; Giessen, H.; Chong, C. T. *Nat. Mater.* **2010**, *9*, 707–715.
- (36) Miroshnichenko, A. E.; Flach, S.; Kivshar, Y. S. *Rev. Mod. Phys.* **2010**, *82*, 2257–2298.